A micro-electro-mechanical accelerometer based on gallium nitride on silicon

C. Morelle, D. Théron, I. Roch-Jeune, Pascal Tilmant, Etienne Okada, F. Vaurette, Bertrand Grimbert, Joff Derluyn, Stefan Degroote, Marianne Germain, et al.

A micro-electro-mechanical accelerometer based on gallium nitride on silicon

C. Morelle[1], D. Theron[1], I. Roch-Jeune[1], P. Tilmant[1], E. Okada[1], F. Vaurette[1], B. Grimbert[1], Joff Derluyn[2], Stefan Degroote[2], Marianne Germain[2], and M. Faucher[1,a)]

[1]*Institut d'Electronique, de Microélectronique et de Nanotechnologie, Univ. Lille, CNRS, Centrale Lille, ISEN, Univ. Valenciennes, UMR 8520 - IEMN, F-59000 Lille, France*

[2]*SOITEC Belgium nv, Kempische steeweg 293, 3500 Hasselt, Belgium*

(a) Author to whom correspondence should be addressed: marc.faucher@univ-lille.fr

We report on an accelerometer micro-sensor based on epitaxial gallium nitride and silicon. The device is a vibrating beam accelerometer (VBA) fabricated with a micro-electro-mechanical-system (MEMS) technology starting from an AlGaN/GaN heterostructure grown on silicon. The vibrating GaN beam has integrated high electron mobility (HEMT) transducers, whereas a high aspect ratio proof mass is engineered in the silicon substrate. The sensor response was investigated for several modes and features a scale factor up to 160 Hz/g, with unconventional dependance versus the mode number. To account for this, we propose an analytical model of the accelerometer scale factor that takes into account the built-in stress during epitaxy. This proof-of-concept device opens perspectives for inertial sensors taking advantage of GaN properties.

Accelerometers based on MEMS are used today in many applications, driven by advances in technologies that have improved figures-of-merits coming with miniaturized sensors[1]. A variety of MEMS accelerometers devices address low-g sensing (seismometry, navigation)[2] to medium ranges (guidance, stabilization) and high-g sensing[3] (shock measurements). In term of mechanical design, two categories can be identified: the pendular accelerometers or the vibrating accelerometers, whereas the transduction can be capacitive[4], piezoresistive[5, 6] or piezoelectric[7]. The high-volume applications make use of silicon pendular devices with capacitive transduction, one reason being the technological simplicity. The vibrating beam accelerometers (VBA) are used in order to target better stability combined to better ranges [1]. Here, the proof mass is linked to a MEMS resonator, whose frequency variation is the sensor readout. Over the past years, high performance VBA accelerometers using quartz or silicon have been developed for inertial navigation [8, 9]. Quartz has a reduced temperature drift of beam frequency and its piezoelectric properties enable to implement resonator actuation and detection. Silicon is more versatile for complex designs due to the maturity of etching techniques[10], but miniaturizing parallel plate transducers for accessing higher resonator frequencies and better sensitivity would face pull-in and stiction issues[11]. Both capacitive and piezoelectric transducers also face limitations for high frequency resonance readouts due to direct signal coupling hiding the motional signal[12]. The need for sensors able to operate in non-standard environments, including high temperatures, and requiring more bandwidth motivates

the exploration of new devices. In this context, we propose to investigate GaN material for resonant accelerometers. III-N materials gather a number of physical properties which potentialities for micro and nano systems have been previously reviewed [13] [14]. In the field of mechanical vibrating devices, our previous work demonstrated how heterostructures based on AlGaN/GaN can be used in actuation and detection [15, 16] .

Here we present a proof-of-concept accelerometer device intending to explore the potentialities of a GaN on silicon substrates. The device architecture is described in Fig. 1. It is composed of a frame, a proof mass and guiding beams made in the silicon substrate. The vibrating beam is defined in the AlGaN/GaN epitaxial stack. One interest of such a hybrid structure is to benefit from a high thickness (265µm) for the proof mass and a small section (20 µm width times 1.8µm thick) for the microresonator, which enable to envision large scale factors with small die sizes. The vibrating beam has integrated transducers. First, actuation is provided by piezoelectric effect inside a capacitor using the two-dimensional electron gas (2-DEG) as a bottom electrode and exploiting the d_{31} coefficient of the AlGaN. Second, on the beam other side a resonant high-electron mobility transistor (R-HEMT) is integrated to provide a stress to current converter. The main feature of such a transducer is to provide amplification by the transistor effect.

The fabrication starts from a 1.8-µm AlGaN/GaN heterostructure grown by MOCVD on a silicon (111) wafer. The fabrication process is similar to those previously reported [17] with the exception of the release process. Here, in order to define the lateral guiding beams and the proof-mass, we patterned the bottom face with a resist mask and we performed a Deep Reactive Ion Etching (DRIE) of Silicon. The final device where sensor characterization has been made is shown on Fig. 2. It differs from the concept of Fig.1 by minor changes in metal routing, and the fact that an additional HEMT amplifier is present. In the following study, only the output of resonant HEMT integrated was used.

Before measurements, the accelerometer was mounted in a metal package. We studied the resonator electromechanical response at atmospheric pressure and room temperature. The R-HEMT was gate and drain-biased using bias tees connected to a sourcemeter. The AC part of the drain-source signal was amplified by a 40 dB factor and sent to a lock-in amplifier to be analyzed (Zurich Instrument UHF-LI). For all the measurements, the transistor is biased with + 2V on the drain and - 5V on the gate. This offers a good compromise between maximization of signal and a moderate drain current of 1,5 mA. The amplitude and phase of the resonator transmission were acquired for the different modes of the beam mechanical vibration (Fig. 3). The quality factor deduced from the width of the resonance is between 315 and 735 for the first four vibration modes. These values are in good agreement with the frequency dependence given by the model of dissipation via air viscous damping at atmospheric

pressure[18]. Secondly, we studied the accelerometer scale factor, defined as the shift of the resonant frequency versus acceleration and expressed in Hz/g where g=9.81 m.s^{-2} (standard acceleration due to gravity).

Usually, such vibrating accelerometers are operated in closed loop. In our case, instead of designing an oscillator for each mode of the vibrating beam, we have chosen to drive the resonator at a fixed frequency and to measure the phase shift under acceleration. This fixed frequency is set without acceleration. The accelerometer scale factor, defined as the frequency increase for a given acceleration in g units, was deduced from the relationship $\Delta f = \Delta\varphi\, f/(2Q)$ where $\Delta\varphi$ is the measured phase shift, Δf the frequency shift, Q the quality factor and f the resonant frequency. The study of the GaN accelerometer scale factor and bandwidth under uniaxial acceleration was performed using an electrodynamic exciter (Brüel & Kjaer 4810). The packaged accelerometer was fixed to the exciter so that the acceleration is applied in the x direction as defined in Fig. 1. A Polytec MSA-500 laser Doppler vibrometer (LDV) was used to calibrate and monitor independently the acceleration given by the electrodynamic exciter. The measurement applying a sinusoidal signal on the resonator actuator at a predetermined resonant frequency (Fig. 3). Then, the electrodynamic exciter was driven with a pure sinusoidal signal at low frequency from 20 Hz to 4 kHz. The Fig 4, inset (a) shows a typical temporal response of the demodulated phase of the detection signal provided by the lock-in. We evidence in FIG. 4. the linear behavior of the accelerometer for a 20 Hz excitation (see also supplementary information). The GaN microresonators with R-HEMT integrated detection delivers enough signal to enable a clear VBA response up to the fourth mode of the beam, reaching working frequencies close to 1 MHz. Following the same experimental procedure, we measured the scale factor for all these modes. The dependence of the scale factor versus frequency of applied acceleration if shown on Fig. 5. We observe that the scale factor is strongly dependent on the mode number, which is not intuitive. First, it should be noticed that the resonant frequencies are higher than it would be expected by the beam dimensions and the Young modulus. This is due to the mean tensile stress resulting from the MOCVD process [19] [20] [21]. Typically for GaN-on-silicon epilayers, a mean stress can be derived from the Stoney formula given a mean bow measured on the wafer after growth. This reaches typical values from 50 to 250 MPa. Due to the accelerometer design, we expect that part of this stress will be relaxed after beam release and a stress σ_0 will remain in the GaN beam. With the presence of σ_0, the resonant frequency of the mode number n can be derived from a modified Euler-Bernoulli equation[22]. Taking into account the boundary conditions for clamped-clamped beams the characteristic equation relating σ_0 and the eigenvalues k_{sn} writes:

$$cosh(k_{sn}^{+})\,cos(k_{sn}^{-}) - \frac{s}{2k_{sn}^{2}}sinh(k_{sn}^{+})\,sin(k_{sn}^{-}) = 1 \quad (1)$$

Here $s = 12\frac{\sigma_0 L^2}{E_{ef}t^2}$ is the normalized stress, and $k_{sn}^{+} = \sqrt{s/2 + \sqrt{s^2/4 + k_{sn}^4}}$ and $k_{sn}^{-} = \sqrt{-s/2 + \sqrt{s^2/4 + k_{sn}^4}}$. The resonance frequency can be deduced from k_{sn} using:

$$f_n = \frac{k_{sn}^2 t}{2\pi L^2}\sqrt{\frac{E_{ef}}{12\rho}} \quad (2)$$

The characteristic equation must be solved implicitly for each value of normalized stress to determine the corresponding eigenvalues k_{sn}. However, f_n can be conveniently written using the eigenvalues without stress k_n:

$$f_n = \frac{k_n^2 t}{2\pi L^2}\sqrt{\frac{E_{ef}}{12\rho}}\sqrt{1 + \frac{\gamma_n' \sigma_0 L^2}{E_{ef}t^2}} \quad (3)$$

The values of γ_n' depend respectively of the mode number. γ_n' is deduced from equations (1) and (2) for each value of stress σ_0 (FIG.). The values of k_n versus the mode number are $k_n \approx 4.73, 7.85, \ldots, (n + 1/2)\pi$. The values of γ_n' have been detailed in ref [23]. γ_n' are equal to $0.2949, 0.1453, \ldots, 12(k_n - 2)/k_n^3$ for $s = 0$ and are slightly stress dependent but the mode number has a stronger influence. With our beam dimensions, γ_n' varies less that 10% for 100 MPa stress. t, L and ρ are respectively the thickness, length and mass density of the beam, and E_{ef} is the effective Young's modulus. Without stress, the frequency increases quadratically with the mode number n, whereas with high tensile stress the dependence is linear.

The applied acceleration a along the x axis creates an inertial force that is balanced both by the resonating beam and the guiding beams. We establish that the stress acting on the vibrating beam due to acceleration is $\sigma_a = c\,Ma/(wt)$ where the factor $c = 0.65$ takes into account the stiffness of the four guiding beams. Here M=295 µg (silicon proof mass). This stress adds to σ_0 in equation (3). The dependance of the vibrating beam resonant frequency versus the applied acceleration can be derived by developing (2) as a Taylor series. This leads to $f_{n,r} = f_n + K_{n,1}a + K_{n,2}a^2 + K_{n,3}a^3 + \cdots$ where $K_{n,1}$ is the scale factor for the n^{th} mode. The following expression is then derived for $K_{n,1}$:

$$K_{n,1} = f_n \frac{cM}{2wt\left(\frac{E_{ef}t^2}{\gamma_n' L^2} + \sigma_0\right)} \tag{4}$$

The expression (4) shows that the presence of stress causes a diminution of the scale factor as compared to the same sensor that would operate rather than without stress. However, the frequency increases with stress and the mode number also adds to the increase of $K_{n,1}$ via the decrease of γ_n' for high n.

In order to be more quantitative in the interpretation of Fig. 5 results, we used the following procedure: starting from known values for ρ, E_{ef}, w, t and L, we deduce σ_0 from equation (3) for the four first modes. We find an average value of 72.8±3.5 MPa. Then for each mode we calculate the scale factor using equation (4). The comparison is shown in FIG. 7. The error bars on the measured values correspond to the four first acceleration frequencies in Fig. 5 (20, 40, 80, 120 Hz). We observe a very good agreement for the first mode with a 6% difference between experiment and modelling. The comparison degrades with the mode number to reach 16% difference for the fourth mode. In order to understand the discrepancy between the experimental values and modeling, we investigated the effect of each parameter on the calculation of the scale factor. From equation (4), we see that the scale factor is proportional to the proof mass M and the inverse of the beam width $1/w$. The other parameters such as ρ, E_{ef}, t and L have a mitigated effect since they also act on the stress σ_0 deduced from equation (3). An increase of the beam thickness reduces the stress deduced from equation (3) which mitigates the effect of t in equation (4) although $1/t$ acts as $1/w$ proportionally on $K_{n,1}$. The beam length uncertainty may have the weakest effect on $K_{n,1}$ since its effect is mitigated by its effect on σ_0. In FIG. 7, we have plotted as error bars, the cumulated effect of a variation of the M and w of 5%. This allows to account for the difference between model and experiment for the three first modes. Uncertainties on other parameters, in particular the beam thickness, may also add to the theoretical error bars and may explain the difference between calculated and experimental values.

The increase of the difference between modelling and measurement with increased mode number indicates that analytical modeling of higher modes may be more inaccurate. In fact, the analytical approach considers that the beam has a uniform density ρ and Young's modulus E_{ef}. In practice, this is not the case since the beam is partially processed with actuation and detection electrodes at the extremities. These electrodes cover about 10 µm on each side of the beam that may modify the effective properties of the beam such as density ρ, Young's modulus E_{ef}. For the first mode, the strain mainly occurs in the

middle of the beam and the extremities have a weak contribution to the beam strain. Increasing the mode number results in nodes with no strain on the beam. In the case of the 4th mode, 3 nodes are present at the quarters and middle of the beam length, which distributes the strain over the beam more regularly. This may increase the influence of the electrodes on the overall properties of the beam and decrease the quality of the analytical modelling. For instance, an increase of the effective Young's modulus E_{ef} and the average density ρ, that may be expected with the presence of electrodes will decrease the deduced stress σ_0 and increase the scale factor as qualitatively observed experimentally compared to modelling. We discuss the effect of the residual stress σ_0 on the scale factor by comparing the experimental values with the scale factor calculated with no stress: In FIG.7 we see that the stress decreases the calculated scale factor by a factor 2.1 on mode 1 but only by a factor 1.35 for mode 4. The compensation of the mode number on the stress effect could make the use of higher modes very attractive to improve the properties of the accelerometer. At high acceleration frequencies, we observe in FIG.5 a reduction of the scale factor. This corresponds to the $f_n/2Q_n$ mechanical bandwidth with the resonator used in this simple open loop measurement technique[24].

Finally, in order to have a first experimental approach of the resolution, Allan deviation measurements have been performed. The curve given in Fig. 8 has been acquired using the third vibration mode of the GaN beam. We evidence a resolution of 0,26 mg/$\sqrt{\text{Hz}}$ with a minimum detection of 2.7 mg. In this experiment the quality factor is limited by the atmospheric pressure, so the resolution should be improved by operating under vacuum. As compared to other published devices [8,25], the main interesting feature of this GaN accelerometer is the gathering of a high scale factor (above 100 Hz/g) coming with a small die size (only 1,5 mm^2), due to the small dimensions of the GaN beam with fully integrated transducers. To assess the full potential of such GaN MEMs devices for VBAs, a next step is required that will use two identical devices matched in a differential configuration. We also emphasis that this study was conducted on a single device and will benefit from gathering data on other devices and from different wafers. Given our previous studies we can anticipate that dispersion in overall accelerometer performances could arise from lithographic dispersion and the initial stress state, linked to epitaxy. In term of measurements, the whole study was conducted during one year without noticing changes of device response.

In summary, a resonant MEMS accelerometer has been demonstrated using GaN and Si. An analytical model has been developed to include the presence of initial tensile stress. This stress implies an increase in frequency, and the higher mode orders can be used without decreasing the performances of the sensor, which implies an even higher increase in frequency,

and an increased bandwidth of the final sensor. Another prospect given by using high tensile stress is that the resolution of the sensor for the different modes will depend mainly on the quality factor, so the mode with higher quality factor can be selected to improve the sensor sensitivity.

ACKNOWLEDGMENTS

This work has been funded by the French National Agency (ANR) with the projects ASTRID AMGASI ANR-11-ASTR-037 01 and NEMSGAN ANR-17-CE09-0036. We also thank the Agence de l'innovation de défense and Région Hauts-de-France for PhD grant financial support. We acknowledge support from labex GANEX (ANR-11-LABX-0014) which belongs to the public funded 'Investissements d'Avenir' program managed by the French ANR agency. We also thank CPER IMITECH and project 'Nanofutur' ANR21-ESRE-0012. This work was also supported by the French RENATECH network.

SUPPLEMENTARY MATERIAL

See supplementary material for the response to the linearity characterization of the resonator modes 1,3,4.

REFERENCES

1 G. Langfelder, M. Bestetti, and M. Gadola, Journal of Micromechanics and Microengineering **31** (8), 084002 (2021).
2 Chen Wang, Fang Chen, Yuan Wang, Sina Sadeghpour, Chenxi Wang, Mathieu Baijot, Rui Esteves, Chun Zhao, Jian Bai, Huafeng Liu, and Michael Kraft, Sensors **20** (14), 4054 (2020).
3 V. Narasimhan, H. Li, and M. Jianmin, Journal of Micromechanics and Microengineering **25** (3), 033001 (2015).
4 D. K. Shaeffer, IEEE Communications Magazine **51** (4), 100 (2013).
5 L. M. Roylance and J. B. Angell, IEEE Transactions on Electron Devices **26** (12), 1911 (1979).
6 A. A. Barlian, W. Park, J. R. Mallon, A. J. Rastegar, and B. L. Pruitt, Proceedings of the IEEE **97** (3), 513 (2009).
7 S. Tadigadapa and K. Mateti, Measurement Science and Technology **20** (9), 092001 (2009).
8 O. Le Traon, J. Guérard, M. Pernice, C. Chartier, P. Lavenus, A. Andrieux, and R. Levy, presented at the 2018 IEEE/ION Position, Location and Navigation Symposium (PLANS), 2018 (unpublished).
9 O. Lefort, I. Thomas, and S. Jaud, presented at the 2017 DGON Inertial Sensors and Systems (ISS), 2017 (unpublished).

[10] Y. Tang, A. Sandoughsaz, K. J. Owen, and K. Najafi, Journal of Microelectromechanical Systems **27** (4), 686 (2018); Michael Huff, Micromachines **12** (8) (2021).
[11] Y. Matsui, Y. Hirai, T. Tsuchiya, and O. Tabata, presented at the 2015 Transducers - 2015 18th International Conference on Solid-State Sensors, Actuators and Microsystems (TRANSDUCERS), 2015 (unpublished).
[12] CJ Van Mullem, HAC Tilmans, AJ Mouthaan, and JHJ Fluitman, Sensors and actuators A: Physical **31** (1-3), 168 (1992).
[13] V. Cimalla, J. Pezoldt, and O. Ambacher, Journal of Physics D: Applied Physics **40** (20), 6386 (2007).
[14] M. Rais-Zadeh, V. J. Gokhale, A. Ansari, M. Faucher, D. Théron, Y. Cordier, and L. Buchaillot, Journal of Microelectromechanical Systems **23** (6), 1252 (2014).
[15] Marc Faucher, Bertrand Grimbert, Yvon Cordier, Nicolas Baron, Arnaud Wilk, Hacène Lahreche, Philippe Bove, Marc François, Pascal Tilmant, Thomas Gehin, Christiane Legrand, Matthieu Werquin, Lionel Buchaillot, Christophe Gaquière, and Didier Théron, Applied Physics Letters **94** (23), 233506 (2009).
[16] Amar Achraf Ben, Faucher Marc, Grimbert Bertrand, Cordier Yvon, François Marc, Tilmant Pascal, Werquin Matthieu, Zhang Victor, Ducatteau Damien, Gaquière Christophe, Buchaillot Lionel, and Théron Didier, Applied Physics Express **5** (6), 067201 (2012).
[17] M. Faucher, Y. Cordier, M. Werquin, L. Buchaillot, C. Gaquiere, and D. Theron, Journal of Microelectromechanical Systems **21** (2), 370 (2012).
[18] F. R. Blom, Journal of Vacuum Science & Technology B: Microelectronics and Nanometer Structures **10** (1), 19 (1992).
[19] A. Dadgar, F. Schulze, T. Zettler, K. Haberland, R. Clos, G. Straßburger, J. Bläsing, A. Diez, and A. Krost, Journal of Crystal Growth **272** (1), 72 (2004).
[20] F. Semond, P. Lorenzini, N. Grandjean, and J. Massies, Applied Physics Letters **78** (3), 335 (2001).
[21] F. Semond, Y. Cordier, N. Grandjean, F. Natali, B. Damilano, S. Vézian, and J. Massies, physica status solidi (a) **188** (2), 501 (2001).
[22] K. Brueckner, V. Cimalla, F. Niebelschütz, R. Stephan, K. Tonisch, O. Ambacher, and M. A. Hein, Journal of Micromechanics and Microengineering **17** (10), 2016 (2007).
[23] Christophe Morelle, Didier Théron, Joff Derluyn, Stefan Degroote, Marianne Germain, Victor Zhang, Lionel Buchaillot, Bertrand Grimbert, Pascal Tilmant, François Vaurette, Isabelle Roch-Jeune, Virginie Brandli, Vanessa Avramovic, Etienne Okada, and Marc Faucher, Microsystem Technologies, 1 (2017).
[24] G. Langfelder and A. Tocchio, IEEE Transactions on Magnetics **50** (1), 1 (2014).
[25] X. Zou, P. Thiruvenkatanathan, and A. A. Seshia, Journal of Microelectromechanical Systems **23** (4), 768 (2014).

FIGURES CAPTIONS

FIG. 1. (a) Concept of the GaN-Silicon hybrid vibrating beam accelerometer (VBA). The silicon substrate is used to define a frame, the proof mass (seismic mass) and in-plane beams ensuring the proof mass guiding. The vibrating beam and the transducers are made using the AlGaN/GaN heterostructure, using GAN as vibrating material and the 2-DEG as bottom electrode for the actuator and active transistor layer for the R-HEMT. (b) Detail of the R-HEMT output transducer. (c) Detail of the piezoelectric actuator.

FIG. 2. Optical image of the accelerometer structure. The vibrating beam is a 390 µm long, 20 µm wide, 1.8 µm thick GaN heterostructure beam. The proof mass and the four guiding beams are made in 260 µm thick silicon.

FIG. 3. Electromechanical characterization of the GaN microresonator. (a) Amplitude of the 2nd mode resonance recorded at the R-HEMT output transducer. (b) phase of the 2nd mode. (c) Quality factor of the four first resonant modes.

FIG. 4. Accelerometer response under electrodynamic excitation. (a): Real time phase of the vibrating beam driven at its second mode 380 kHz resonant frequency. The applied acceleration magnitude is 640 mg at 20 Hz. (b) accelerometer response studied for 3 decades of acceleration.

FIG. 5. Dependence of the scale factor Bode plot versus mode order. Measurements were taken at 100 mg acceleration.

FIG. 6. Evolution of γ'_n with the normalized stress s for the four first modes.

FIG. 7. Comparison between experimental and analytically modeled scale factor $K_{n,1}$ for the four first modes ($n = 1$ to 4). For comparison, the theoretical values for the same resonant frequency without initial stress are shown. The error bars on experimental values correspond to the four lowest acceleration frequencies in Fig.5. The error bars on calculated values corresponds to 5% variation of the proof mass cumulated with 5% variation of the beam width.

FIG. 8. Allan deviation for the mode 3 for 300 mV actuation. The measurement was performed with 10 kHz bandwidth and 54 k-samples/s.

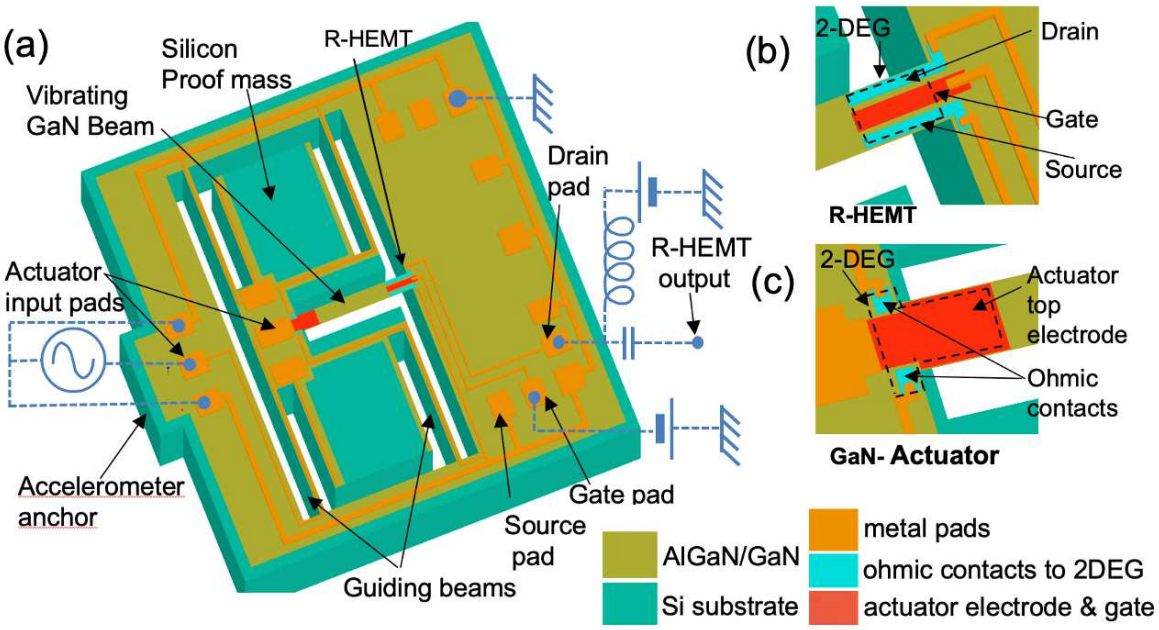

PLEASE CITE THIS ARTICLE AS DOI: 10.1063/5.0127987

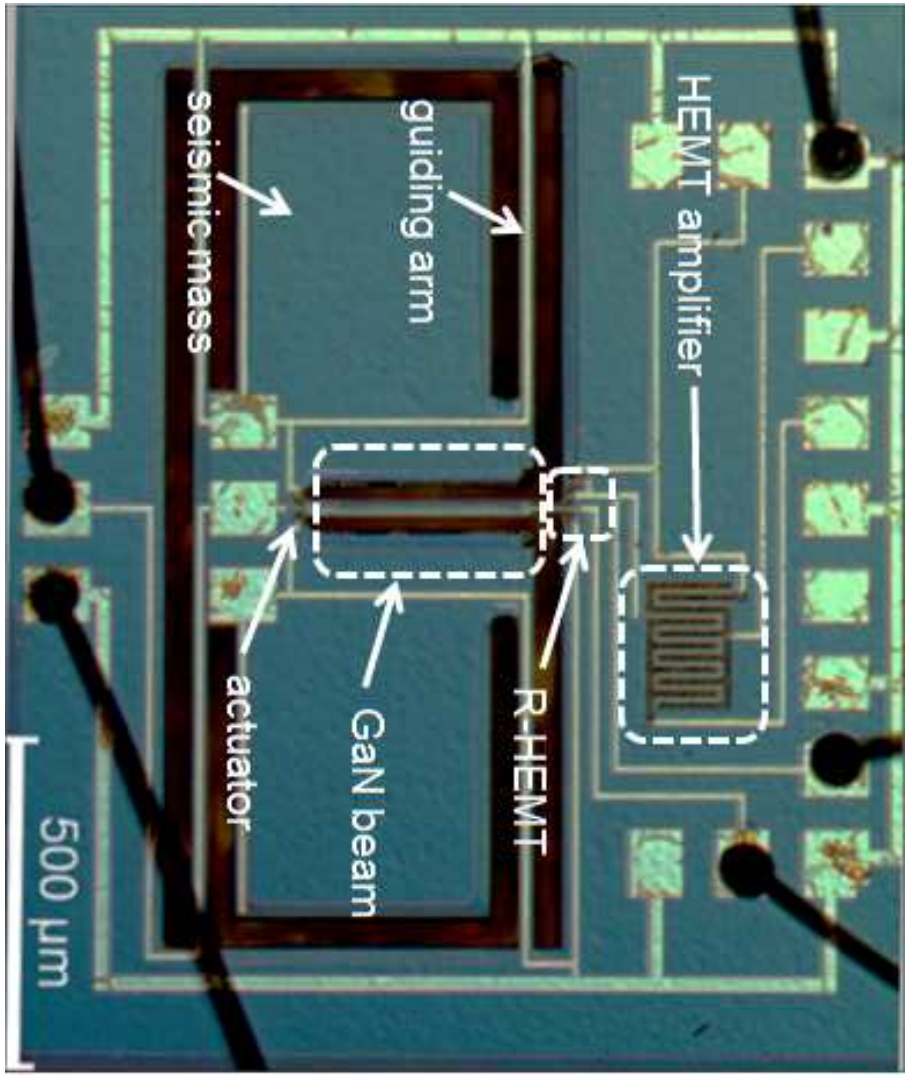

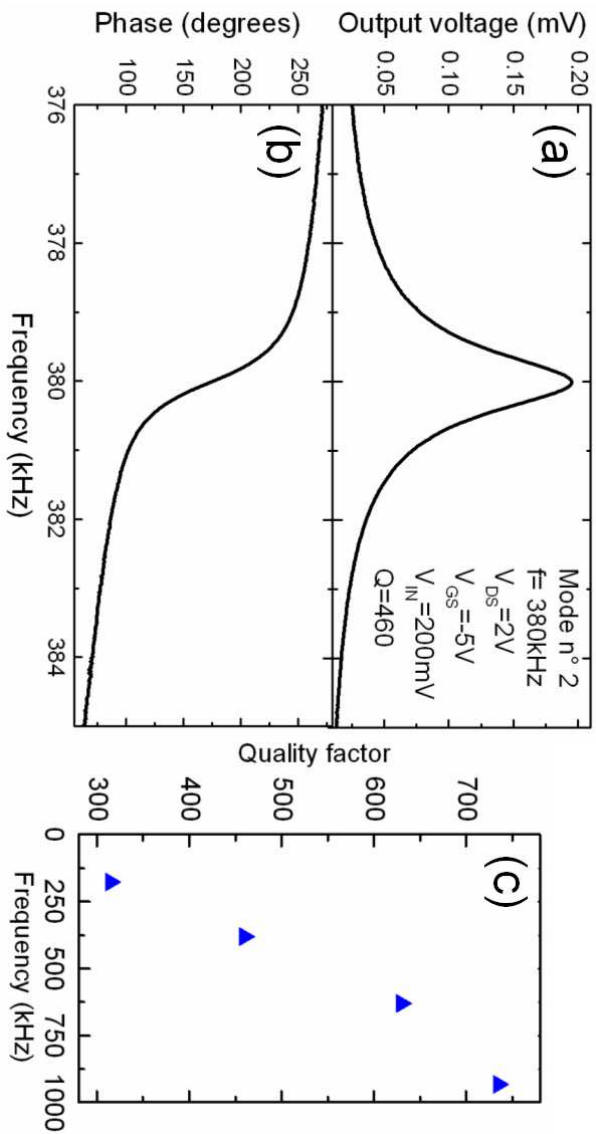

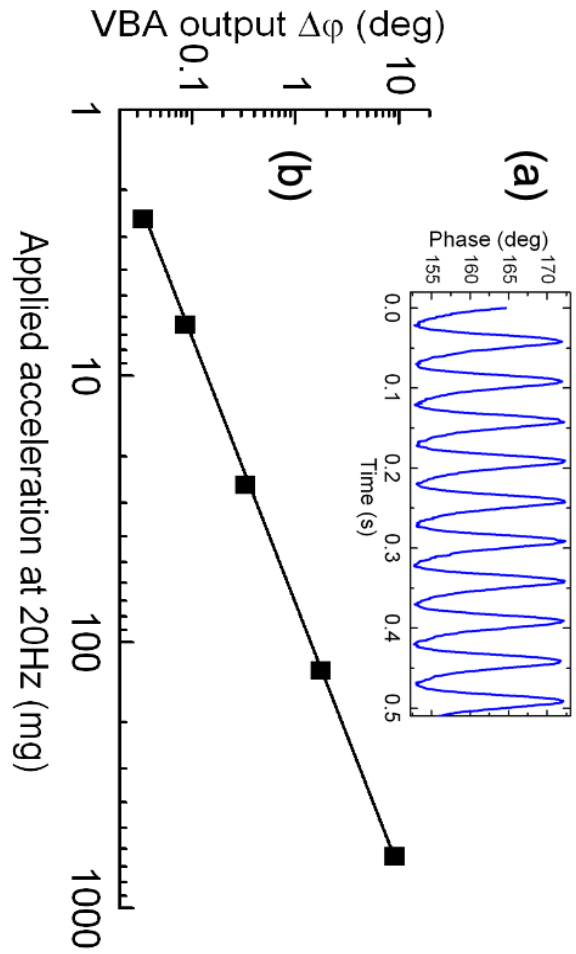

Applied Physics Letters

PLEASE CITE THIS ARTICLE AS DOI: 10.1063/5.0127987

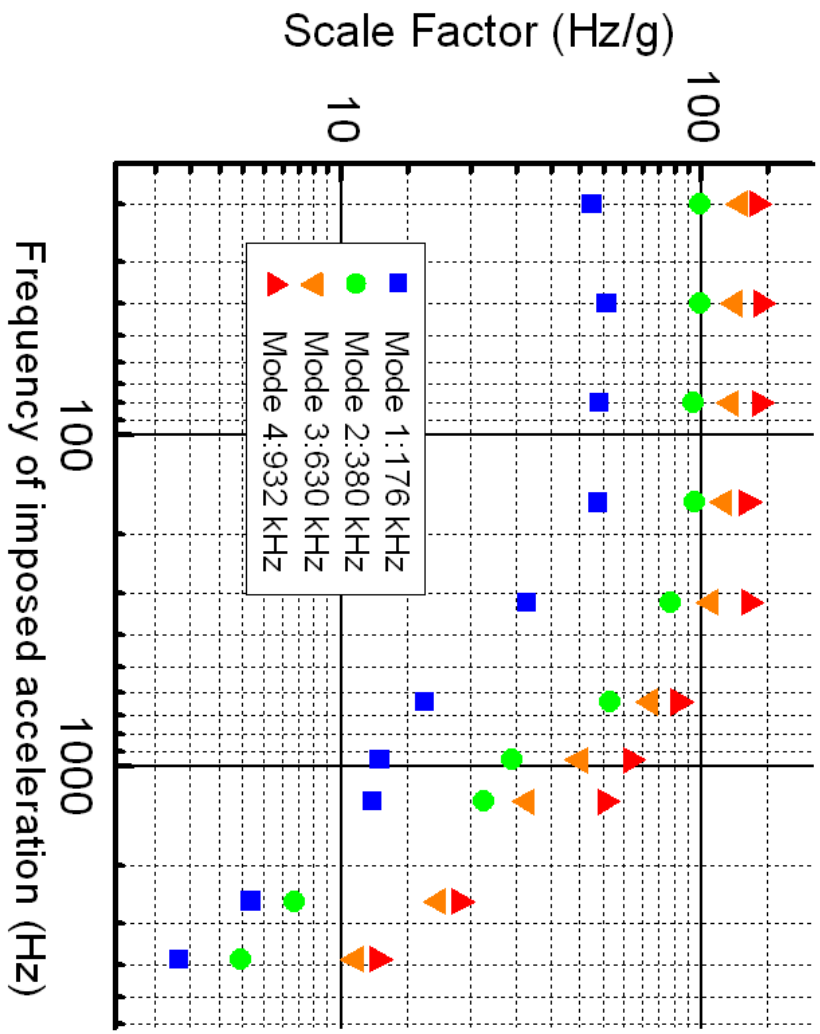

Applied Physics Letters

PLEASE CITE THIS ARTICLE AS DOI: 10.1063/5.0127987

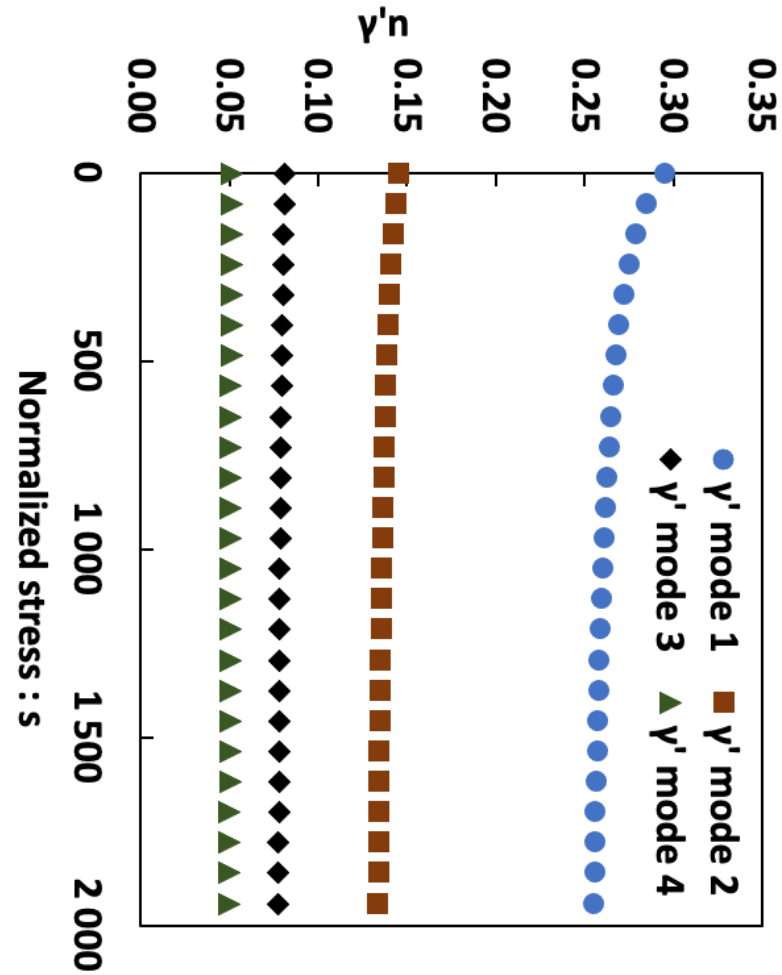

Applied Physics Letters

PLEASE CITE THIS ARTICLE AS DOI: 10.1063/5.0127987